Unraveling the dynamics and structure of functionalized self-assembled monolayers on gold using 2D IR spectroscopy and MD simulations

Chang Yan[a,1], Rongfeng Yuan[a,1], William C. Pfalzgraff[a,1], Jun Nishida[a], Lu Wang[a], Thomas E. Markland[a], and Michael D. Fayer[a,2]

[a]Department of Chemistry, Stanford University, Stanford, CA 94305

Contributed by Michael D. Fayer, February 26, 2016 (sent for review January 26, 2016; reviewed by Eric Borguet, Steven A. Corcelli, and Kenneth B. Eisenthal)

Functionalized self-assembled monolayers (SAMs) are the focus of ongoing investigations because they can be chemically tuned to control their structure and dynamics for a wide variety of applications, including electrochemistry, catalysis, and as models of biological interfaces. Here we combine reflection 2D infrared vibrational echo spectroscopy (R-2D IR) and molecular dynamics simulations to determine the relationship between the structures of functionalized alkanethiol SAMs on gold surfaces and their underlying molecular motions on timescales of tens to hundreds of picoseconds. We find that at higher head group density, the monolayers have more disorder in the alkyl chain packing and faster dynamics. The dynamics of alkanethiol SAMs on gold are much slower than the dynamics of alkylsiloxane SAMs on silica. Using the simulations, we assess how the different molecular motions of the alkyl chain monolayers give rise to the dynamics observed in the experiments.

self-assembled monolayer | dynamics | 2D IR spectroscopy | MD simulation

Self-assembled monolayers (SAMs) on planar metal surfaces enable the tailoring of interfacial properties by functionalization of the alkyl chains. SAMs formed by alkanethiol chains on gold surfaces are of particular interest due to the ordered packing of the chains, chemical stability, and facile methods of preparation, as well as the diverse array of chemical functionalization that can be added (1). The properties of SAMs on gold have led to applications including electrochemical devices (2), surface patterning (3), model biological surfaces (4), and heterogeneous catalysis (5). In many of these applications, the interfacial properties of the monolayer are determined largely by the particular head group linked at the terminal site of the alkyl chain.

The structure of SAMs on gold has been well characterized by scanning probe microscopy (6), helium diffraction (7), X-ray photoelectron spectroscopy (8), sum-frequency generation spectroscopy (SFG) (9), and linear infrared spectroscopy (10). However, to determine how the physical and chemical properties of SAMs are related to their microscopic dynamics and structure and the influence of head groups present in most applications, fast time-resolved experimental techniques, with sufficient selectivity and sensitivity, are required to measure the structural dynamics of a monolayer of molecules on the appropriate picosecond (ps) timescale.

Two-dimensional infrared vibrational echo spectroscopy (2D IR) provides the necessary observables by measuring spectral diffusion, i.e., the time-dependent evolution of the probe vibrational frequency in response to structural fluctuations of the chemical environment (11–13). To use 2D IR to investigate monolayer dynamics requires selectivity for the interfacial region. One method to achieve this is to combine 2D IR spectroscopy with SFG (14, 15), which requires a vibrational mode that has both a large IR transition dipole and a large Raman cross-section. However, for a monolayer functionalized with the vibrational probe, 2D IR is inherently interface-selective, and SFG is not required. In prior work, 2D IR spectroscopy in the standard transmission mode was used to investigate vibrational probe functionalized alkyl monolayers on a thin SiO_2 layer deposited on an IR transparent substrate (16, 17). The 2D IR of monolayers in the transmission mode is limited to IR transparent substrates. Hamm and coworkers recently combined 2D IR with attenuated total reflection (ATR), allowing them to observe the dynamics of an azide vibrational probe functionalized alkyl chains on sputtered polycrystalline gold surfaces (18). The azide head groups, with a vibrational lifetime of ∼1 ps, provided surface-selective measurements of the spectral diffusion at the monolayer's terminal sites for a few picoseconds. The monolayers were immersed in several solvents, and the azide head group probed the interfacial interactions between the monolayer and solvent molecules. However, the short vibrational lifetime made it difficult to capture details of the surface layer dynamics, such as the dynamics of alkyl chains, which occur on timescales of tens to hundreds of picoseconds.

Here, we developed and applied 2D IR spectroscopy directly by operating in the reflection mode, R-2D IR, which can be conveniently used for a wide range of reflective bulk metal surfaces in addition to sputtered layers of metals. Combined with a long-lived metal carbonyl vibrational probe as the head group, we are able to observe the dynamics of functionalized undecanethiol (C11 chain) monolayers grown on crystalline Au(111) surfaces to 40 ps. By measuring the dynamics as a function of head group density, we find that reducing the head group density at constant chain density changes the structure, producing a more ordered monolayer with slower dynamics. The experimental results

Significance

Self-assembled monolayers (SAMs) are a form of nanotechnology that enables the functionalization of surfaces with single layers of chemically designed structures having tuned properties. In contrast to the characterization of time-average static structures, it is challenging to measure the dynamic behavior of SAMs on the timescales of molecular motions, i.e. picoseconds. Here we combine 2D IR spectroscopy and molecular dynamics (MD) simulations to investigate alkyl chain monolayers functionalized with a head group. The dynamics reported by the head group are induced by the alkyl chain motions. For example, it was determined that SAMs with higher alkyl chain gauche defect content have faster dynamics caused by more frequent chain conformational fluctuations.

Author contributions: C.Y., W.C.P., T.E.M., and M.D.F. designed research; C.Y., R.Y., W.C.P., and J.N. performed research; C.Y. and R.Y. contributed new reagents/analytic tools; C.Y., R.Y., W.C.P., L.W., T.E.M., and M.D.F. analyzed data; and C.Y., W.C.P., T.E.M., and M.D.F. wrote the paper.

Reviewers: E.B., Temple University; S.A.C., University of Notre Dame; and K.B.E., Columbia University.

The authors declare no conflict of interest.

See Commentary on page 4890.

[1]C.Y., R.Y., and W.C.P. contributed equally to this work.

[2]To whom correspondence should be addressed. Email: fayer@stanford.edu.

This article contains supporting information online at www.pnas.org/lookup/suppl/doi:10.1073/pnas.1603080113/-/DCSupplemental.

are compared with molecular dynamics (MD) simulations, which show very good agreement with the structure and dynamics measured in IR experiments. These simulations demonstrate that the motions of the head group vibrational probes are caused by the dynamical rearrangement of the alkyl chain monolayers on timescales ranging from tens to hundreds of picoseconds, and that a variety of alkyl chain motions play an important role in the observed spectral diffusion of head groups. The monolayers with more gauche defects have more frequent chain conformation changes and therefore faster dynamics as observed in the simulations and experiments.

Static Structure of Gold SAMs

To understand the interplay of structure and dynamics first the static structures were characterized. The monolayers studied consist of undecanethiol alkyl chains that are chemically bound to an Au(111) surface. After the deposition of alkyl chains, the rhenium carbonyl vibrational probe (*fac*-Re(phenC≡CH)$(CO)_3$Cl) is attached to the monolayer via a Cu(I)-catalyzed alkyne-azide cycloaddition (CuAAC) reaction ("click" chemistry). In addition to the head group rhenium carbonyl complex (the vibrational probe), there is also a triazole ring, which is formed during the cycloaddition reaction (Fig. 1*A*). The synthesis and characterization of the monolayers are described in the *Supporting Information*. To assess the effect of head group density with constant chain density on the structure and fast dynamics, we prepared monolayers with two different head group densities, 1.9×10^{14} cm^{-2} determined using inductively coupled plasma mass spectrometry (ICP-MS), which corresponds to the largest number of head groups that can be attached to the surface, and 0.9×10^{14} cm^{-2}, corresponding to about half of the maximum head group density. The higher head group (HG) density system is abbreviated HG_{high}, and the lower head group density system is HG_{low}. Taking the alkyl chain density in alkanethiol SAMs to be 4.67×10^{14} cm^{-2} (17, 19), the fraction of chains that are functionalized with head groups in the monolayers was ~40% for HG_{high} and ~20% for the HG_{low}. Based on the ICP-MS–measured head group density, the distance between two adjacent rhenium centers is calculated to be 0.75 nm for HG_{high} and 1.09 nm for HG_{low}. In the experimental samples, the head groups in the HG_{high} samples are essentially closely packed with an even distribution. The head groups are large enough that once one is attached some adjacent chains are blocked from functionalization. In the HG_{low} samples, the head groups are essentially randomly distributed (17, 19). In the MD simulations, the head groups are attached to the gold on an evenly spaced periodic grid, chosen to reproduce the experimental density.

Fig. 1*B* shows the normalized Fourier transform infrared (FT-IR) spectra of the vibrational probe carbonyl symmetric stretching mode region for the two head group density samples. The difference in peak frequency is the first indication that changing the head group density influences the monolayer structure. The full widths at half maximum of both peaks are ~21 cm^{-1}. To measure the orientation of the head groups relative to the surface, we performed the polarization resolved FT-IR experiments on this mode, which measure an average orientational order parameter $\langle S \rangle = 1/2(3\langle \cos^2\theta_{HG} \rangle - 1)$, where θ_{HG} is the angle between the transition dipole moment of the symmetric CO stretching mode of the head group, $\vec{\mu}$, and the surface normal (Fig. 1*A*). The measurement of $\langle S \rangle$ provides an experimental measure of this angle, $\bar{\theta}_{HG}$, and the relationship between these quantities is described in more detail in the *Supporting Information*. For HG_{high} we obtained $\bar{\theta}_{HG} = 54 \pm 3°$, and for HG_{low}, $\bar{\theta}_{HG} = 42 \pm 3°$. These results show that the head group density influences the monolayer structure.

To unravel how the atomistic details of these monolayer systems give rise to the experimental structure observables, MD simulations of the functionalized SAMs (described in the *Supporting Information*) at both densities were performed. The MD simulations gave $\bar{\theta}_{HG} = 62 \pm 1°$ for HG_{high} and $\bar{\theta}_{HG} = 54 \pm 1°$ for HG_{low}, in reasonably good agreement with the experiment. Of particular importance is that the simulations show the change in structure with head group density. Using simulations, we can analyze the orientational distribution of θ_{HG} that gives rise to the experimentally observed average orientational order parameters, $\langle S \rangle$ and $\bar{\theta}_{HG}$. In Fig. 2*A*, the MD simulations of HG_{low} indicate that 80% of the functionalized chains have a θ_{HG} of ~40°, but there is also a minority of functionalized chains, around 20%, that have θ_{HG} ~110°. This minor subensemble has the transition dipoles pointing toward the substrate. In the simulation, head groups with a θ_{HG} of ~40° have the phenanthroline ring oriented almost parallel to the surface, whereas head groups with an θ_{HG} of ~110° have their phenanthroline rings oriented almost perpendicular to the surface (Fig. 2*A*). Therefore, in HG_{low} the majority

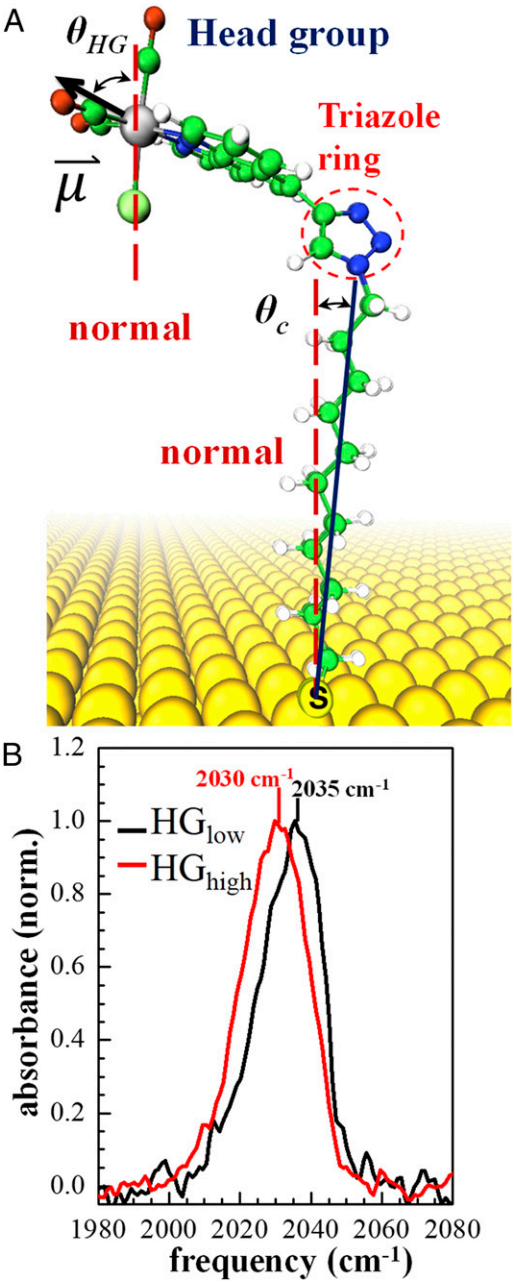

Fig. 1. (*A*) Schematic illustration of a single functionalized undecanethiol chain, and the orientation angles defined for the head group and alkyl chain. (*B*) Normalized linear infrared absorption spectra of the carbonyl symmetric stretching mode.

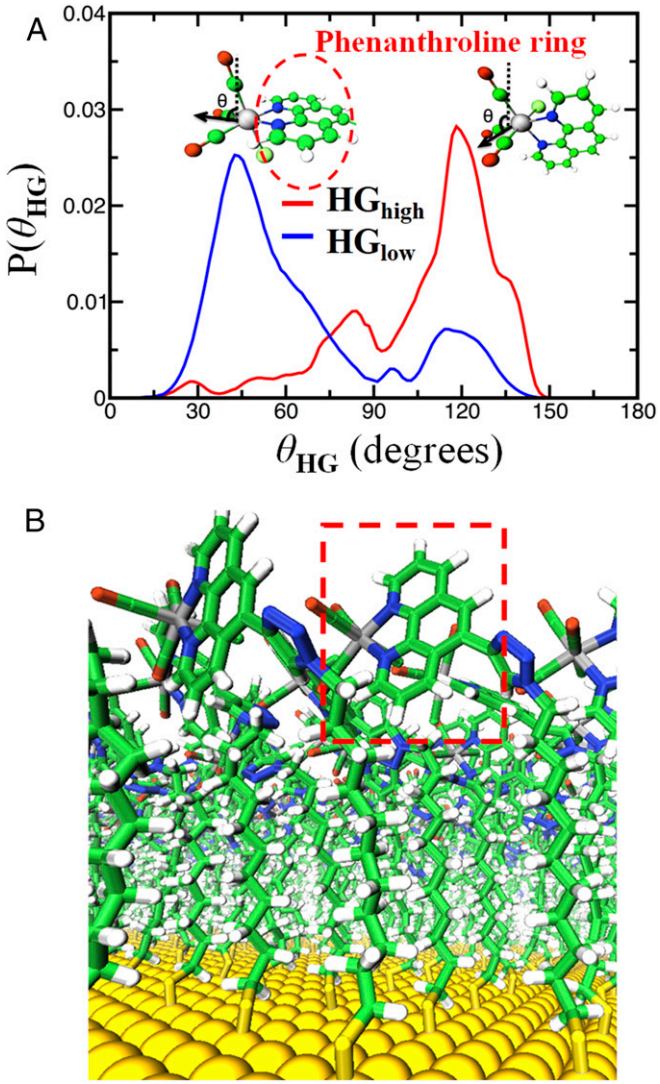

Fig. 2. (*A*) Distributions of angles that give rise to the observed $\overline{\theta}_{HG}$. Angles near 40° have a head group with the phenanthroline ring primarily orientated parallel to the gold surface; whereas, angles near 110° have the phenanthroline rings primarily oriented perpendicular to the planar surface. (*B*) MD simulation box for HG_{high} showing head groups with the perpendicular orientation.

of the functionalized alkyl chains have phenanthroline rings oriented parallel to the surface. In contrast, in the HG_{high} simulation with much higher head group density, 76% of functionalized chains' phenanthroline rings are oriented perpendicular to the surface with $\theta_{HG} > 90°$, although only a minority have the parallel orientation. The perpendicular orientation minimizes steric hindrance between adjacent head groups, allowing many more head groups to be packed into the same area. In Fig. 2*B*, a snapshot of the simulation for HG_{high} illustrates that the majority of the head groups are packed in the perpendicular orientation. The red-dashed rectangle marks a particular head group with the perpendicular orientation. The change in surface coverage, which results in distinct head group orientation distributions for HG_{high} and HG_{low}, is likely responsible for the difference in the IR absorption center frequencies for HG_{low} and HG_{high} (Fig. 1*B*). Both the widths of the IR absorption peaks and the widths of head group orientation distributions are almost the same for the two kinds of SAMs. This suggests that for a given SAM, the distribution of head group orientations can be an important inhomogeneous broadening mechanism.

From simulations, we can also extract the tilt angle of the alkyl chains, θ_c, relative to the surface normal, which is illustrated in Fig. 1*A*. The steric hindrance between head groups can affect this tilt angle. The HG_{low} simulation has an average chain tilt angle of 37 ± 2°, in good agreement with previous experimental (1) and theoretical (20) work on unfunctionalized gold SAMs (~30°). In contrast, the simulation of HG_{high} yields $\theta_c = 11 \pm 1°$. The head group interactions in the denser HG_{high} force the alkyl chains to orient in a more upright fashion, deviating significantly from the tilt angle of well-packed unfunctionalized SAMs on gold. The different packing of the alkyl chains for HG_{high} increases the number of gauche defects in the chains as the chain geometry must accommodate the steric interactions among the head groups. The degree of ordered packing in monolayers can be determined by monitoring the C–H stretching region of linear infrared absorption spectra (21–23). For both densities, the peak center of the methylene (-CH_2-) antisymmetric stretching mode was located at ~2,920 cm^{-1}, which indicates ordered chain packing with a low percentage of gauche defects, as a large number of gauche defects shifts this peak to higher frequency (23–25). In the HG_{low} simulation, 6% of the alkyl chain methylenes have gauche defects, whereas the percentage is 15% for the HG_{high} monolayers. Thus, the chains have a relatively small percentage of gauche defects, consistent with experiment, although the higher head group density sample, HG_{high}, has more gauche defects and a smaller chain tilt angle than HG_{low}.

Probing the Dynamics Using Reflection 2D IR Spectroscopy and Molecular Simulation

Having characterized the static structures of these systems, we now examine the structural dynamics of the monolayer and how the different head group densities give rise to different dynamics. The head group carbonyl symmetric stretch vibrational absorption line is inhomogeneously broadened because of the range of structures that result in different intermolecular interactions of the vibrational probes with their surroundings. Structural fluctuations cause the probes' vibrational frequencies to evolve with time within the inhomogeneously broadened absorption line (spectral diffusion). To probe the dynamics, we used 2D IR spectroscopy to measure the spectral diffusion. In a 2D IR experiment, three infrared pulses (denoted as pulse 1, 2, and 3 in temporal sequence), which selectively excite the carbonyl symmetric stretching mode, were focused and overlapped spatially on the monolayer surface using the Box Coherent Anti-Stokes Raman Spectroscopy (BOXCARS) geometry. The time period between pulse 1 and pulse 2 is denoted as τ and the time period between pulse 2 and pulse 3 is denoted as T_w. The interaction of the three pulses with sample leads to the emission of the vibrational echo pulse in the wave vector matched direction. The echo was combined with an external local oscillator pulse (LO) to provide heterodyne detection and phase information. The combined echo/LO pulse is resolved by a spectrograph equipped with a 32-pixel array detector. At a fixed T_w, τ is scanned to generate a time domain interferogram for each array pixel (ω_m). Each interferogram was then Fourier transformed to yield the ω_τ axis (horizontal axis) in the 2D spectrum; ω_m is the vertical axis.

Hence, at each T_w, a 2D spectrum is obtained. The dynamical information is contained in the change in shape of the 2D spectrum with T_w. Qualitatively, the first two pulses in the sequence label and store the initial frequencies (ω_τ axis) of the vibrational probes. During the period T_w, the structure and therefore the frequencies evolve. The third pulse and the echo read out the final frequencies (ω_m axis), permitting the frequency evolution and therefore the structural evolution to be observed. The decay of the correlation between the initial and final vibrational frequencies is expressed by the frequency–frequency correlation function (FFCF). The FFCF was extracted from the 2D line shape via the center line slope (CLS), which is the T_w-dependent portion of the normalized FFCF (24, 25). To obtain the CLS, a series of cuts is taken through the

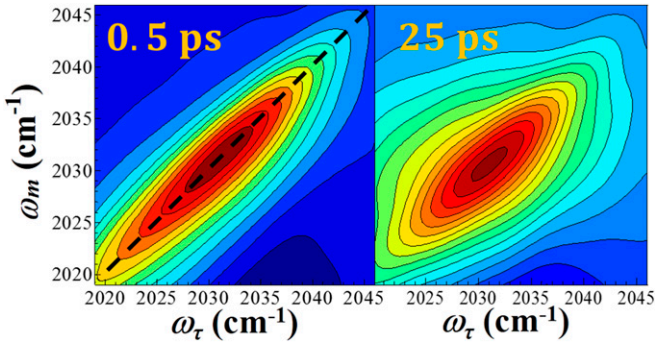

Fig. 3. The 2D IR spectra from the HG_{high} monolayer at waiting times, T_w = 0.5 and 25 ps. The dynamical information is contained in the change in the shape of the 2D spectrum with T_w. The dashed line in *Left* is the diagonal.

2D spectrum near the 2D band center parallel to the ω_m axis for a range of ω_τ. Each cut is a 1D spectrum, the center line consists of the set of points that are located at the peaks of the 1D spectra obtained from the cuts, and the CLS is the slope of this line. At short T_w, the CLS is close to unity, with the spectrum elongated along the diagonal, (the dashed line in Fig. 3, *Left*). The elongation shows there is a high correlation between ω_τ and ω_m. As T_w increases, the loss of frequency correlation because of structural evolution causes the 2D spectrum to become more round (Fig. 3, *Right*), and the CLS decreases. The spectral diffusion is measured by the time-dependent decay of CLS values as T_w increases. The CLS (normalized FFCF) decay curves are usually modeled with a multiexponential function (12, 24–28). The time constants of the exponential terms provide the timescales of the ensemble average fluctuations that contribute to spectral diffusion rather than the rate of a particular structural event.

To perform the experiments on gold substrates, we developed R-2D IR. In this technique, the three excitation pulses and the echo pulse are reflected from the gold surface, which is essentially perfectly reflecting in the IR. The *s*-polarized component of the electric field at the monolayer surface of an excitation pulse vanishes because of the interference of incident and reflected electric fields. Therefore, it is necessary to rotate the gold substrate, changing each pulse's composition of *p* and *s* polarization, to an optimal angle. As the sample is rotated, the *p* component increases, increasing the signal, but the area of the laser spot becomes larger, decreasing the electric field of each pulse and the signal. However, the larger area laser spot encompasses more vibrational probes, increasing the signal. There is an optimal angle, ~58°, which maximizes the signal. The calculation of the optimal tilt angle is given in the *Supporting Information*.

Fig. 3 shows R-2D IR spectra for the HG_{high} SAM at T_w = 0.5 and 25 ps. The spectra focus on the 0–1 vibrational transition region (red, positive signal); a portion of the 1–2 region (blue, negative signal) can be seen below the 0–1 spectrum. All the information of interest here is obtained from the 0–1 region. At T_w = 0.5 ps (Fig. 3, *Left*), the spectrum is elongated along the diagonal (dashed line), showing high correlation between frequencies of ω_τ and ω_m. The calculated CLS values for both HG_{high} and HG_{low} are ~0.85 at T_w = 0.5 ps, demonstrating that inhomogeneous broadening, rather than homogeneous broadening, dominates the absorption spectrum. The homogeneous line widths were determined to be 3.9 and 3.2 cm^{-1} for HG_{high} and HG_{low}, respectively, which are small compared with the total linewidths of 21 cm^{-1}. At T_w = 25 ps (Fig. 3, *Right*), the 2D IR spectrum has changed shape, but the change is not large, indicating that the spectral diffusion is relatively slow. The carbonyl symmetric stretching mode of the rhenium complex head group has a vibrational relaxation lifetime of 11 ps, as measured by the heterodyne-detected transient grating (HDTG) technique (16, 17). The relatively long vibrational relaxation lifetime enables observation of spectral diffusion for the SAMs to T_w = 40 ps.

The normalized experimental CLS decay data for HG_{high} and HG_{low} are shown in Fig. 4 (red points). Both CLS curves can be fit (red solid curves) with single exponential decays. The experimental spectral diffusion time constants for HG_{high} and HG_{low} are 83 ± 2 ps and 98 ± 5 ps, respectively. These are the timescales for structural fluctuations that cause the vibrational probes to sample frequencies in the inhomogeneously broadened absorption spectrum.

In the MD simulations, the frequency fluctuations can be modeled in terms of electric field fluctuations. The electric field model has been shown to be successful in calculating the FFCF (spectral diffusion) from classical MD simulations (26–28). To compare with the experimental CLS, the autocorrelation function of the electric field from all components of the monolayer projected along the head group's carbonyl symmetric stretching mode transition dipole vector was computed. We used this electric field–electric field correlation function (EECF) and a Stark tuning constant to calculate the FFCF, which was in turn used to compute the response functions for simulating the 2D IR spectra (24, 25). Using the calculated 2D IR spectra as a function of T_w, the CLS decay curves were obtained from the simulations (blue points in Fig. 4). The simulated data (blue points) were fit with single exponential decay functions (blue curves). In the simulation the $RePhen(CO)_3Cl$ moiety is treated as a classical rigid body, which means that the simulation does not probe ultrafast motions of the head group itself, which may contribute to the homogeneous linewidth. Because we are interested in dynamics on timescales that are relevant to monolayer molecular conformational motions (~tens of picoseconds), we are only concerned with spectral diffusion and not the homogenous dephasing. Therefore, in Fig. 4 all CLS curves were normalized by dividing by the initial CLS value at the earliest T_w of each curve.

As seen in Fig. 4, the agreement in timescales of spectral diffusion between theory and simulation is very good, demonstrating that the simulations capture the essential molecular motions that are observed in the experiments. The experimental time constant is 83 ± 2 ps compared with the simulated value of 100 ± 10 ps for

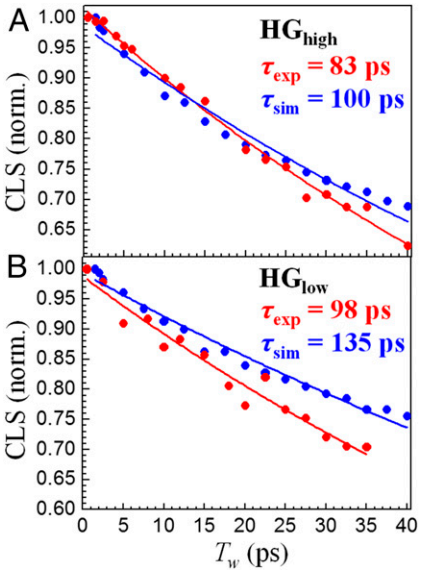

Fig. 4. Experimental (red) and simulated (blue) normalized CLS decay curves of (*A*) HG_{high} and (*B*) HG_{low}. The solid curves are the single exponential fits for the measured and simulated CLS decay curves.

HG_{high}, and for HG_{low} the experimental time constant is 98 ± 5 ps and the simulated time constant is 135 ± 15 ps. The simulations capture the fact that the spectral diffusion slows when the head group density is decreased.

Given that the simulations show that the structure of HG_{high} is more disordered than HG_{low} (as indicated by higher chain tilt angle and increased percentage of gauche defects), the simulation results demonstrate that the monolayers with more ordered chain packing have slower dynamics, as measured by the spectral diffusion. This is consistent with previous work on functionalized undecylsiloxane monolayers on amorphous SiO_2, where even faster spectral diffusion time constants of ∼40 ps were observed (17). The undecyl chains on amorphous SiO_2 have many more gauche defects compared with their undecanethiol on gold counterparts. The increase in gauche defects is shown by the fact that on SiO_2 the C–H anti-symmetric stretching mode appears at 2,925 cm^{-1} (17). The weak Au–S bonds in SAMs on gold facilitate the migration of alkanethiol chains so that highly ordered packing can be achieved via a facile 2D "recrystallization" process (1), which is not possible in the alkylsiloxane SAMs due to the strong Si–O bonds. The net result is a picture in which the packing of chains on SiO_2 is more disordered, facilitating faster structural evolution and faster spectral diffusion.

Determining the Origins of Spectral Diffusion in Gold SAMs

To gain insights into the origins of the spectral diffusion, we examined details of the simulated electric field correlation function. The EECF is closely related to the 2D IR spectral diffusion observable, the CLS, but not identical, and the CLS can be obtained from the EECF using the procedure described above (24, 25). First, we decomposed the simulated EECF into contributions from the different components of the system, which are shown in the *Supporting Information* (27, 29–31). This decomposition reveals that the EECF of a given head group has two major contributing components that have nearly equal weights: the electric fields arising from the phenanthroline rings of the rhenium complex anchored on the nearest-neighbor chains, and the electric fields from triazole rings anchored on the nearest-neighbor chains. The sum of all of the remaining contributions to the EECF (including the Re atom, neighboring CO and Cl ligands, and the alkyl chains) is nearly zero for both HG_{high} and HG_{low}.

To assess what motions these decomposed EECF contributions correspond to, we compared them to other characteristic correlation functions of motion in the system. We find that at both densities, the portion of the EECF that comes from neighboring phenanthroline rings is nearly identical in shape and timescale to the orientational autocorrelation function of the carbonyl symmetric stretching transition dipole vector, i.e., orientational motions of the head groups. Both the in-plane wiggle and out-of-plane wobble orientational dynamics of the rhenium complex take place on the timescale of ∼110 ps for the high density sample. The portion of the EECF that comes from the triazole component has a nearly identical shape and timescale to that of the triazole dihedral autocorrelation function, which is related to rotation of the triazole ring relative to the underlying alkyl chains (*Supporting Information*). Therefore, the simulation reveals that the electric fields fluctuations that are measured by the spectral diffusion come primarily from the orientational motion of the rhenium complex, as well as the rotational motion of the triazole ring.

Because of the chemical attachment of the head groups to the alkyl chains, the head group and triazole ring motions that cause spectral diffusion can be driven by the underlying chains, even though the alkyl chains' electric fields only contribute a negligible component directly to the total EECF. To assess the extent of this coupling, we performed a simulation in which we increased the mass of all of the alkyl chains by a factor of 10, leaving the mass of the head groups unchanged (described in the *Supporting Information*). This change decreases the average speed of all of the atoms in the alkyl chain by a factor of $1/\sqrt{m}$ ∼0.316, but has no effect on the structural properties of the simulation. If the alkyl chains and head group possess strongly coupled dynamics, then the increased mass of the chains would increase the observed spectral diffusion time constant. Alternately, if the head group spectral diffusion is not influenced by the underlying chain motions, increasing the mass would have no effect on the simulated 2D IR spectra. In the simulations, increasing the mass slows down the spectral diffusion by a factor of ∼1.3, with the simulated spectral diffusion time constant of HG_{high} increased from 100 to 135 ps, and that of HG_{low} increased from 135 to 170 ps. This result demonstrates that the motion of the alkyl chains and the spectral diffusion of the head groups are coupled.

We next consider which dynamical events in the alkyl chains lead to spectral diffusion. Although there are a large number of types of chain motions, we will focus on two well-defined distinct events. In the simulation, alkyl chains in the monolayer undergo frequent conformational changes arising from dihedral flips (changes in the carbon chain torsional angle) between the gauche and anti-conformers. These dihedral flips occur on average every 18 ps for HG_{high} and every 24 ps for HG_{low}. In addition, the chains also undergo triazole rearrangements, in which the triazole ring rotates between its dihedral minima relative to the alkyl chain. The effects of these motions on the structure are shown in the *Supporting Information*. Triazole rearrangements occur every 74 ps on average for HG_{high} and every 92 ps on average for HG_{low}. Notably, the frequency of both of these events is about ∼30% lower in the HG_{low} simulations, which is similar to the increase in the spectral diffusion time constant in the HG_{low} simulations. The slowing of spectral diffusion is also consistent with the fact that HG_{low} has a lower percentage of gauche defects in the alkyl chains. Because dihedral flips and triazole rearrangements occur on similar timescales as the experimental spectral diffusion, we assessed the role of these events.

To assess whether dihedral flip and triazole rearrangement events are reported on by the experimentally observed spectral diffusion, we calculated the conditional EECF of HG_{high} following one of these events happening at time $t = 0$. That is, we consider the subensemble of trajectories in which that particular event occurred at $t = 0$, and calculate the conditional EECF by averaging only over this subensemble. If the occurrence of the event is not coupled to the spectral diffusion, then the EECF will be unchanged when averaging over this subensemble. In contrast, if the event is coupled to the spectral diffusion, then the conditional EECF will decay either slower or faster depending on whether it hinders or aids spectral diffusion.

We first applied this approach to dihedral flips. Because dihedral flips can occur at many different positions in the 11-carbon alkyl chain, to assess how far down the chain these events are reported in the spectral diffusion we calculated the conditional EECFs as a function of dihedral position in the chain. In particular, to create the subensemble used to compute the conditional EECF we considered whether a dihedral flip had occurred in the top part of the chain (the first three carbon dihedrals closest to the triazole ring), the middle (carbon dihedrals 4–6), or the bottom part of the chain (carbon dihedrals 7–10). The conditional EECF time constants are 85 ps for the top of the chain, 102 ps for the middle of the chain, and 135 ps for the bottom of the chain. Therefore, dihedral flips in the top and middle parts of the chain decrease the decay time constant of the EECF from ∼110 to ∼80–100 ps in the conditional EECF, indicating that dihedral flips in the top and middle parts of the alkyl chain lead to rapid spectral diffusion. In contrast, rearrangements on the bottom portion of the chains contribute less to the spectral diffusion than the monolayer dynamics in the top half of the chains.

It is important to recognize what these results mean about chain dynamics. In the averaging of trajectories following a dihedral flip, $t = 0$ is the frame following the flip. Therefore, the

flip itself and any electric field change associated with the actual flip are not included in the trajectories. The results demonstrate that a dihedral flip induces other chain motions, both on the chain on which the flip occurs and likely on adjacent chains, i.e., that the dihedral flip event triggers motions that cause spectral diffusion on the experimental (tens of picoseconds) timescale.

We also applied this approach to triazole rearrangement events. The conditional EECF when a triazole rearrangement occurred in the frame immediately before $t = 0$ had a time constant of 80 ps, which is significantly faster than 110 ps for the EECF. Again, the implication is that the triazole rearrangement causes other chain motions that are responsible for the increased rate of spectral diffusion. From these analyses, we conclude that the spectral diffusion reflects an averaging over many types of chain dynamics, and that dihedral flips and triazole rearrangements contribute to spectral diffusion by driving subsequent chain motions.

Concluding Remarks

Here we have investigated the structure and dynamics of SAMs on Au(111) surfaces that are functionalized with a head group that also serves as the vibrational probe for ultrafast 2D IR experiments and MD simulations. To perform the experiments, 2D IR spectroscopy was advanced to work in a reflection mode. The structural dynamics of alkyl chains were tracked by measuring the spectral diffusion of the carbonyl symmetric stretching mode of the vibrational probe. MD simulations showed very good agreement with the experimental measurements of both dynamics and structure. The dynamics occur on the tens to hundreds of picoseconds timescales, and increasing the head group density at fixed chain density changes both the structure and the dynamics of the monolayer. At maximum head group density, simulations show that the chain tilt angle is 11°, but when the head group density is cut in half, the tilt angle becomes 37°, in agreement with previously measured values in the absence of head groups. Simulations also showed that the higher head group density SAMs have more alkyl chain gauche defects (15%) compared with the lower head group density SAMs with 6% gauche defects, consistent with experiments that show a small number of gauche defects. In addition, the structural dynamics measured by 2D IR and calculated with the simulations are slower when the head group density is reduced. These results demonstrate the impact of functionalization of the alkyl chains with bulky head groups, which occurs in most applications. For both head group densities, simulations demonstrate that there are a number of dynamical processes that contribute to spectral diffusion, including dihedral flips in the alkyl chain backbone and triazole ring flips. The rates of these processes decrease when the head group density and the concomitant gauche defect content are decreased, consistent with the observed slowdown in the spectral diffusion. The results presented here provide a detailed picture of the dynamics and structure of functionalized SAMs at the molecular level, including how the presence of head groups can influence both structure and dynamics.

ACKNOWLEDGMENTS. We thank Ming Gong for performing X-ray diffraction measurements on the Au(111) substrate. This work was supported by the Air Force Office of Scientific Research Grant FA9550-16-1-0104 (to C.Y., R.Y., J.N., and M.D.F.) and by the US Department of Energy, Office of Science, Office of Basic Energy Sciences, under Award DE-SC0014437 (to W.C.P., L.W., and T.E.M.). T.E.M. also acknowledges support from a Cottrell Scholarship from the Research Corporation for Science Advancement and an Alfred P. Sloan Research Fellowship. C.Y., W.C.P., and J.N. thank the Stanford Graduate Fellowship program for financial support, and L.W. acknowledges support from a fellowship from the Stanford Center for Molecular Analysis and Design.

1. Love JC, Estroff LA, Kriebel JK, Nuzzo RG, Whitesides GM (2005) Self-assembled monolayers of thiolates on metals as a form of nanotechnology. *Chem Rev* 105(4):1103–1169.
2. Neuhausen AB, Hosseini A, Sulpizio JA, Chidsey CED, Goldhaber-Gordon D (2012) Molecular junctions of self-assembled monolayers with conducting polymer contacts. *ACS Nano* 6(11):9920–9931.
3. Liao WS, et al. (2012) Subtractive patterning via chemical lift-off lithography. *Science* 337(6101):1517–1521.
4. Ostuni E, Grzybowski BA, Mrksich M, Roberts CS, Whitesides GM (2003) Adsorption of proteins to hydrophobic sites on mixed self-assembled monolayers. *Langmuir* 19(5): 1861–1872.
5. Schoenbaum CA, Schwartz DK, Medlin JW (2014) Controlling the surface environment of heterogeneous catalysts using self-assembled monolayers. *Acc Chem Res* 47(4):1438–1445.
6. Poirier GE (1997) Characterization of organosulfur molecular monolayers on Au(111) using scanning tunneling microscopy. *Chem Rev* 97(4):1117–1128.
7. Camillone N, Chidsey CED, Liu GY, Putvinski TM, Scoles G (1991) Surface-structure and thermal motion of normal-alkane thiols self-assembled on Au(111) studied by low-energy helium diffraction. *J Chem Phys* 94(12):8493–8502.
8. Folkers JP, Laibinis PE, Whitesides GM (1992) Self-assembled monolayers of alkanethiols on gold - Comparisons of monolayers containing mixtures of short-chain and long-chain constituents with CH_3 and CH_2OH terminal groups. *Langmuir* 8(5):1330–1341.
9. Lahann J, et al. (2003) A reversibly switching surface. *Science* 299(5605):371–374.
10. Allara DL, Parikh AN, Rondelez F (1995) Evidence for a unique chain organization in long-chain silane monolayers deposited on 2 widely different solid substrates. *Langmuir* 11(7):2357–2360.
11. Cho M (2008) Coherent two-dimensional optical spectroscopy. *Chem Rev* 108(4):1331–1418.
12. Park S, Kwak K, Fayer MD (2007) Ultrafast 2D-IR vibrational echo spectroscopy: A probe of molecular dynamics. *Laser Phys Lett* 4(10):704–718.
13. Hamm P, Zanni MT (2011) *Concepts and Methods of 2D Infrared Spectroscopy* (Cambridge Univ Press, Cambridge).
14. Xiong W, Laaser JE, Mehlenbacher RD, Zanni MT (2011) Adding a dimension to the infrared spectra of interfaces using heterodyne detected 2D sum-frequency generation (HD 2D SFG) spectroscopy. *Proc Natl Acad Sci USA* 108(52):20902–20907.
15. Zhang Z, Piatkowski L, Bakker HJ, Bonn M (2011) Ultrafast vibrational energy transfer at the water/air interface revealed by two-dimensional surface vibrational spectroscopy. *Nat Chem* 3(11):888–893.
16. Rosenfeld DE, Gengeliczki Z, Smith BJ, Stack TDP, Fayer MD (2011) Structural dynamics of a catalytic monolayer probed by ultrafast 2D IR vibrational echoes. *Science* 334(6056):634–639.
17. Yan C, Yuan RF, Nishida J, Fayer MD (2015) Structural influences on the fast dynamics of alkylsiloxane monolayers on SiO_2 surfaces measured with 2D IR spectroscopy. *J Phys Chem C* 119(29):16811–16823.
18. Kraack JP, Lotti D, Hamm P (2015) 2D attenuated total reflectance infrared spectroscopy reveals ultrafast vibrational dynamics of organic monolayers at metal-liquid interfaces. *J Chem Phys* 142(21):212413.
19. Collman JP, Devaraj NK, Eberspacher TPA, Chidsey CED (2006) Mixed azide-terminated monolayers: A platform for modifying electrode surfaces. *Langmuir* 22(6):2457–2464.
20. Cossaro A, et al. (2008) X-ray diffraction and computation yield the structure of alkanethiols on gold(111). *Science* 321(5891):943–946.
21. Hamoudi H, Dablemont C, Esaulov VA (2011) Disorder, solvent effects and substitutional self-assembly of alkane dithiols from alkane thiol SAMs. *Surf Sci* 605(1-2):116–120.
22. Macphail RA, Strauss HL, Snyder RG, Elliger CA (1984) C-H stretching modes and the structure of normal-alkyl chains. 2. Long, all-trans chains. *J Phys Chem* 88(3):334–341.
23. Snyder RG, Strauss HL, Elliger CA (1982) C-H stretching modes and the structure of normal-alkyl chains. 1. Long, disordered chains. *J Phys Chem* 86(26):5145–5150.
24. Kwak K, Park S, Finkelstein IJ, Fayer MD (2007) Frequency-frequency correlation functions and apodization in two-dimensional infrared vibrational echo spectroscopy: A new approach. *J Chem Phys* 127:124503.
25. Kwak K, Rosenfeld DE, Fayer MD (2008) Taking apart the two-dimensional infrared vibrational echo spectra: More information and elimination of distortions. *J Chem Phys* 128(20):204505.
26. Corcelli SA, Lawrence CP, Skinner JL (2004) Combined electronic structure/molecular dynamics approach for ultrafast infrared spectroscopy of dilute HOD in liquid H_2O and D_2O. *J Chem Phys* 120(17):8107–8117.
27. Merchant KA, et al. (2003) Myoglobin-CO substate structures and dynamics: Multidimensional vibrational echoes and molecular dynamics simulations. *J Am Chem Soc* 125(45):13804–13818.
28. Bagchi S, Boxer SG, Fayer MD (2012) Ribonuclease S dynamics measured using a nitrile label with 2D IR vibrational echo spectroscopy. *J Phys Chem B* 116(13):4034–4042.
29. Nilsson L, Halle B (2005) Molecular origin of time-dependent fluorescence shifts in proteins. *Proc Natl Acad Sci USA* 102(39):13867–13872.
30. Kobrak MN, Znamenskiy V (2004) Solvation dynamics of room-temperature ionic liquids: Evidence for collective solvent motion on sub-picosecond timescales. *Chem Phys Lett* 395(1-3):127–132.
31. Furse KE, Corcelli SA (2010) Molecular dynamics simulations of DNA solvation dynamics. *J Phys Chem Lett* 1(12):1813–1820.
32. Nishida J, Fayer MD (2014) Theory of third-order spectroscopic methods to extract detailed molecular orientational dynamics for planar surfaces and other uniaxial systems. *J Chem Phys* 140(14):144702.
33. Vanommeslaeghe K, et al. (2010) CHARMM general force field: A force field for drug-like molecules compatible with the CHARMM all-atom additive biological force fields. *J Comput Chem* 31(4):671–690.
34. Devi J (2014) Aggregation of thiol coated gold nanoparticles: A simulation study on the effect of polymer coverage density and solvent. *Comput Mater Sci* 86:174–179.
35. Plimpton S (1995) Fast parallel algorithms for short-range molecular dynamics. *J Comput Phys* 117:1–19.
36. Yeh I-C, Berkowitz ML (1999) Ewald summation for systems with slab geometry. *J Chem Phys* 111:3155–3162.

Supporting Information

Yan et al. 10.1073/pnas.1603080113

Optical Setup

The 2D IR and HDTG experiments were conducted with the same optical platform. Midinfrared pulses (duration ~170 fs, bandwidth of 90 cm^{-1}, pulse energy ~5.5 μJ, center at ~2,025 cm^{-1}) were generated at 1 kHz with an optical parametric amplifier pumped by a regeneratively amplified Ti:Sapphire laser system. The vibrational echo pulse was combined with an external LO pulse to provide heterodyne detection and phase information.

Sample Fabrication and Characterization

Sample Fabrication of HG_{high} and HG_{low}. All commercial solvents and reagents were used as received. The 11-bromo-1-undecanethiol (99%), 1-undecanethiol (98%), sodium azide (99.5%), copper(II) sulfate pentahydrate (99.999%), tris(2-pyridylmethyl)amine (98%), and sodium L-ascorbate (98%) were purchased from Sigma-Aldrich. Toluene (99%), deionized and ultrafiltered water, and chloroform (99.9%) were purchased from Fischer Scientific. Ethanol (99.5%), and dimethylformamide (DMF, 99.8%) were purchased from ACROS. DMSO (99.9%) was purchased from EMD Millipore. The highly crystalline gold substrate with Au(111) surface was purchased from Sigma-Aldrich and was used as received. The gold layer was 100 nm in thickness and was deposited onto a Si(100) wafer with an adhesion layer of titanium in between.

Before monolayer deposition, the gold substrate was cleaned by sonication in toluene and ethanol for 3 min each. The substrate was then dried by a flow of clean, dry nitrogen gas; 10 μL of the 11-bromo-1-undecanethiol was injected into 12.5 mL of ethanol, then the gold substrate was immersed in the solution for 24 h at room temperature. After deposition, the wafer was isolated, and rinsed thoroughly with ethanol, toluene, and ethanol in sequence. The substrate was then dried by a flow of nitrogen gas. The terminal bromine atoms of the formed alkylthiolate monolayers were replaced by azide groups through a nucleophilic substitution, which was performed by immersing the monolayer sample in a saturated solution of sodium azide in DMF for 24 h. After the substitution, the gold substrate was rinsed sequentially in DMF, water, and ethanol, then dried by nitrogen. Success of the substitution was checked by the infrared absorption of the azide stretching mode (peak height ~0.4 m.O.D) at 2,100 cm^{-1}. The beam incident angle used in the FT-IR measurement was 60°. The rhenium carbonyl complex, *fac*-Re(phenC ≡ CH)(CO_3)Cl, was synthesized according to the previous literature (16). A copper-catalyzed azide–alkyne cycloaddition (CuAAC) was used to immobilize the rhenium complex head group at the terminal site of the monolayers. A 2:1 vol/vol DMSO/water solution containing the rhenium complex (0.3 mM), $CuSO_4$ (0.3 mM), tris(2-pyridylmethyl)amine (0.3 mM), sodium L-ascorbate (3 mM, 10 equiv per Cu) was prepared and purged with N_2. The azide-functionalized substrate was then submerged and the solution was capped for 2 d at room temperature. After the reaction, the gold substrate was removed, rinsed sequentially by copious amount of 2:1 DMSO/water mixture, DMSO, water, and ethanol to remove residual reactants. Then the substrate was immersed in chloroform for 1 h to clean up any nonbonded rhenium complex, which may embed in the monolayer producing an extra red wing in infrared spectrum. Finally the wafer was rinsed by ethanol, and dried by nitrogen. The success of terminal site functionalization was checked by infrared absorption spectroscopy and ICP-MS of rhenium. The measurement of surface coverage of the head group was described in the sections below.

The prepared monolayer samples were stored in dark and were cleaned by rinsing with ethanol and toluene before spectroscopic measurements were performed. There was no decay in the samples' infrared absorption signal level after several months of storage and multiple cleaning cycles.

The procedures above are for HG_{high}. For HG_{low}, at the monolayer deposition step, instead of injecting 10 μL of 11-bromo-1-undecanethiol into 12.5 mL of ethanol, we used a 12.5 mL ethanol solution containing 5 μL of 11-bromo-1-undecanethiol and 5 μL of 1-undecanethiol. The rest of the preparation of HG_{low} monolayer is essentially the same as the procedures for HG_{high} monolayer.

Inductively Coupled Plasma Mass Spectrometry. The total rhenium content of a monolayer sample was measured by ICP-MS on a Thermo Scientific XSERIES 2 ICP-MS instrument. To digest the sample, the monolayer is covered with 1.5 mL of 70% nitric acid (HNO_3) for 12 h, then the solution is quantitatively transferred into a 25 mL volumetric flask. A series of standard solutions of rhenium were made in the 1–50 ppb range to use for calibration.

Infrared Absorption Spectroscopy. The infrared absorption spectra of the monolayers were recorded with 1 cm^{-1} resolution with a Nicolet 6700 FT-IR spectrometer purged with clean air free of oil, water vapor, and CO_2. For SAMs on gold, the absorption spectra were collected with a *p*-polarized beam in a homemade reflection mode setup at incident angle 60°, using a blank gold wafer as the background. For alkylsiloxane monolayers on silica, the unpolarized and polarization resolved absorption spectra were collected in the transmission mode.

X-ray Diffraction Measurement. The X-ray diffraction (XRD) measurement of the Au(111) on silicon substrate was performed on a PANalytical X'Pert instrument with Cu Kα line. In Fig. S1, the (111) texture of Au was confirmed by the diffraction peak at 38.2°.

The Extraction of Transition Dipole Orientation of the Head Group's Carbonyl Symmetric Stretching Mode

Generalized Consideration for the Infrared Absorption of the Monolayer Samples Measured in Transmission Mode. A model for the linear IR absorption of the anisotropic monolayer samples in transmission mode is shown in Fig. S2. Transition dipole orientation (red arrow) is defined by two angles θ and φ, which are the polar and azimuthal angles with respect to the surface normal (green arrow), respectively. Incident beams (blue arrow), including the scenarios of both *s*- and *p*-polarized light, arrive at the sample with the incident angle ϕ. We note the unitary pointing vector of the electric field of the excitation beam as $\vec{E}(x,y,z)$, with $|\vec{E}|^2 = 1$. The integrated peak area of absorbance A is independent of the power of excitation beam, and is directly proportional to the absolute interaction between the electric field vector and transition dipole, per unit area within the excitation beam. Here, we express the absolute interaction for a single dipole at a specific orientation as the dot product of the transition dipole vector and the electric field vector: $|\mu|^2|\hat{\mu}(\theta,\varphi)\cdot\vec{E}|^2$, where $\hat{\mu}(\theta,\varphi)$ is the unitary vector representing the orientation of transition dipole and $|\mu|$ is the transition dipole moment of the head group's carbonyl symmetric stretching mode.

We designated $P_{\hat{\mu}}(\theta,\varphi)$ as the distribution of dipole orientation, and therefore A is proportional to the integrated interaction between light and dipole across all of the possible orientations, as shown in Eq. **S1**:

$$A \propto \rho|\mu|^2 \iint d\theta d\varphi P_{\hat{\mu}}(\theta,\varphi)\left(\hat{\mu}(\theta,\varphi)\cdot\vec{E}\right)^2 = C\cdot\rho|\mu|^2 \iint d\theta d\varphi P_{\hat{\mu}}(\theta,\varphi)\left(\hat{\mu}(\theta,\varphi)\cdot\vec{E}\right)^2, \quad \textbf{[S1]}$$

where ρ is the surface density of the head group, C is a scaling factor that is independent from the experimental parameters of different measurements discussed in this paper.

We further project $\hat{\mu}(\theta,\varphi)$ and $\vec{E}$ onto the three orthogonal axis x, y, and z, as shown in Fig. S2. The real part of $\vec{E}$ can be expressed as the vector $(|\vec{E}_x|, |\vec{E}_y|, |\vec{E}_z|)$ and $\hat{\mu}(\theta,\varphi)$ can be expressed as $(\sin\theta\cos\varphi, \sin\theta\sin\varphi, \cos\theta)$. Therefore, we have:

$$\begin{aligned} A &= C\cdot\rho|\mu|^2 \int_0^{\pi} d\theta P_{\hat{\mu}}(\theta)\frac{1}{2\pi}\int_0^{2\pi} d\varphi\left(\left|\vec{E}_x\right|^2\sin^2\theta\cos^2\varphi + \left|\vec{E}_y\right|^2\sin^2\theta\sin^2\varphi + \left|\vec{E}_z\right|^2\cos^2\theta\right) \\ &= C\cdot\rho|\mu|^2 \int_0^{\pi} d\theta P_{\hat{\mu}}(\theta)\left(\left(\frac{\left|\vec{E}_x\right|^2}{2}+\frac{\left|\vec{E}_y\right|^2}{2}\right)\sin^2\theta + \left|\vec{E}_z\right|^2\cos^2\theta\right). \end{aligned} \quad \textbf{[S2]}$$

In the monolayer sample, φ has an isotropic distribution from 0 to 2π, and θ is approximated by a very narrow distribution. We express $P_{\hat{\mu}}(\theta,\varphi)$ as follows: $P_{\hat{\mu}}(\theta,\varphi) \triangleq \frac{1}{2\pi}\delta(\theta)$. For our sample, unless the distribution range of θ is exceptionally large (half cone angle > 50°), the above expression is a good approximation for calculating the average of θ (17, 32). Then Eq. **S1** transforms into the following form:

$$A = C\cdot\rho|\mu|^2\left(\left(\frac{\left|\vec{E}_x\right|^2}{2}+\frac{\left|\vec{E}_y\right|^2}{2}\right)\sin^2\bar{\theta} + \left|\vec{E}_z\right|^2\cos^2\bar{\theta}\right). \quad \textbf{[S3]}$$

For unpolarized FT-IR spectra, the incident angle is $\phi = 0°$, and the unpolarized beam has an equal amount of *s*- and *p*-polarized component. For *s*-polarized light, $|\vec{E}_x| = 1$, and $|\vec{E}_y| = |\vec{E}_z| = 0$. For *p*-polarized beam, $|\vec{E}_x| = 0$, $|\vec{E}_y| = \cos\phi = 1$ and $|\vec{E}_z| = \sin\phi = 0$. Therefore, by Eq. **S3**, we can derive that the integrated absorbance is: $A_{SiO_2,unp} = C\cdot\rho_{SiO_2}|\mu|^2\frac{1}{2}\sin^2\bar{\theta}_{SiO_2}$, where ρ_{SiO_2} and $\bar{\theta}_{SiO_2}$ are the surface density and the average transition dipole orientation of head groups on the alkylsiloxane monolayer.

In the polarization-resolved FT-IR, the spectra of *s*- or *p*-polarized beams were both measured at $\phi = 45°$. Due to oblique incidence, the number of excited head group per unit area increases by a factor of $1/\cos\phi = \sqrt{2}$. For *s*-polarized beam, by Eq. **S3**, the integrated absorbance is: $A_{SiO_2,S} = C\cdot\rho_{SiO_2}|\mu|^2\frac{\sqrt{2}}{2}\sin^2\bar{\theta}_{SiO_2}$. For *p*-polarized beam, the integrated absorbance is: $A_{SiO_2,P} = C\cdot\sqrt{2}\rho_{SiO_2}|\mu|^2\left(\frac{1}{4}\sin^2\bar{\theta}_{SiO_2} + \frac{1}{2}\cos^2\bar{\theta}_{SiO_2}\right)$.

From the results of above, the ratio between the integrated absorbance for *s*- and *p*-polarized spectra is: $R_{SP,SiO_2} = \frac{A_{SiO_2,S}}{A_{SiO_2,P}} = \frac{2\sin^2\bar{\theta}_{SiO_2}}{1+\cos^2\bar{\theta}_{SiO_2}}$. Therefore, the average transition dipole orientation angle $\bar{\theta}_{SiO_2}$ can be derived as following:

$$\cos^2\bar{\theta}_{SiO_2} = \frac{2R_{SP,SiO_2}-2}{3\left(R_{SP,SiO_2}-\frac{3}{2}R_{SP,SiO_2}-1\right)}+\frac{1}{3}$$

$$\bar{\theta}_{SiO_2} = \arccos\left(\frac{2R_{SP,SiO_2}-2}{3\left(R_{SP,SiO_2}-\frac{3}{2}R_{SP,SiO_2}-1\right)}+\frac{1}{3}\right)^{1/2}. \quad \textbf{[S4]}$$

The Extraction of the Average Transition Dipole Orientation Angle of Alkylthiolate Monolayers on Au(111). Because the thickness of a monolayer sample is around a few nanometers, the distance from the head group to the gold substrate is only a negligible portion of the wavelength of mid-IR beam at ~2,000 cm^{-1}. Therefore, the carbonyl symmetric stretching mode of head group is essentially excited by the electric field at surface, which is the interference of the incident and reflected beams.

Near the gold (treated as a perfect conductor) surface, the overall electric field is the sum of the incident and reflected beam: $\vec{E}_{local}(y,z) = \vec{E}_i(y,z) + \vec{E}_r(y,z)$. Refer to Fig. S2 for the coordinate system.

For *s*-polarized beam, the surface electric field vector is described by Eq. **S5**:

$$\begin{aligned} \vec{E}_{local,S}(y,z) &= \vec{x}\cdot|E_0|\left(e^{-jBz\cos\phi} - e^{jBz\cos\phi}\right)\cdot e^{-jBy\sin\phi} \\ &= -\vec{x}\cdot|E_0|j\cdot 2\sin(Bz\cos\phi)\cdot e^{-jBy\sin\phi}, \end{aligned} \quad \textbf{[S5]}$$

where $\vec{x}$ is the unitary vector pointing along the x axis, B is the propagation constant of the beam, and $|E_0|$ is the amplitude of electric field of the incident beam.

For *p*-polarized beam, the surface electric field vector is described by Eq. **S6**:

$$\begin{aligned} \vec{E}_{local,P}(y,z) &= \vec{y}\cdot\cos\phi\cdot|E_0|\left(e^{-jBz\cos\phi} - e^{jBz\cos\phi}\right)\cdot e^{-jBy\cdot\sin\phi} \\ &\quad -\vec{z}\cdot\sin\phi\cdot|E_0|\left(e^{-jBz\cos\phi} + e^{jBz\cos\phi}\right)\cdot e^{-jBy\cdot\sin\phi} \\ &= \left[-\vec{y}\cdot|E_0|j\cdot 2\cos\phi\sin(Bz\cos\phi)\right. \\ &\quad \left. -\vec{z}\cdot|E_0|2\sin\phi\cos(Bz\cos\phi)\right]\cdot e^{-jBy\cdot\sin\phi}, \end{aligned} \quad \textbf{[S6]}$$

where $\vec{y}$ and $\vec{z}$ are the unitary vectors pointing along the y and z axis, respectively.

At the surface, $z = 0$, by Eqs. **S5** and **S6**, we have: $\vec{E}_{local,S}(y,z) = 0$ and $\vec{E}_{local,P}(y,z) = -\vec{z}\cdot|E_0|2\sin\phi\cdot e^{-jBy\cdot\sin\phi}$. The *s*-polarized component completely vanishes at the surface. For *p*-polarized beam, the transversely oscillating component vanishes and the normal component is doubled. The doubled component will enhance the absorbance by a factor of $4\sin^2\phi$.

The FT-IR measurement in reflection mode was performed using *p*-polarized beam at $\phi = 60°$. Therefore, by Eq. **S3** and the discussions above, the integrated absorbance of the head groups of alkylthiolate monolayers on Au(111) is as follows:

$$A_{Au} = C\cdot 4\sin^2\phi\cdot\frac{1}{\cos\phi}\cdot\rho_{Au}|\mu|^2\cos^2\bar{\theta}_{Au} = 6\rho_{Au}|\mu|^2\cos^2\bar{\theta}_{Au}. \quad \textbf{[S7]}$$

By Eq. **S7** and the previous section, we have: $\frac{A_{SiO_2,unp}}{A_{Au}} = \frac{\frac{1}{2}\sin^2\bar{\theta}_{SiO_2}}{6\cos^2\bar{\theta}_{Au}}\frac{\rho_{SiO_2}}{\rho_{Au}}\frac{|\mu|^2}{|\mu|^2}$.

The head group surface densities ρ_{SiO_2} and ρ_{Au} are determined by ICP-MS; $\bar{\theta}_{SiO_2}$ is determined by the polarization-resolved FT-IR discussed in the previous section. Because we use the same head group for monolayers on SiO_2 or Au(111), the transition dipole moment $|\mu|$ is the same for both forms of monolayers. Finally, we can derive $\bar{\theta}_{Au}$ as follows:

$$\bar{\theta}_{Au} = \arccos\left(\frac{A_{Au}}{A_{SiO_2,unp}}\frac{\sin^2\bar{\theta}_{SiO_2}}{12}\frac{\rho_{SiO_2}}{\rho_{Au}}\right)^{1/2}. \quad \textbf{[S8]}$$

Optimization of the Sample Tilting Angle for Reflection 2D IR Under BOXCARS Geometry by Numerical Simulation

Coordinate System and General Description of the Model. A Cartesian coordinate system is set up as shown in Fig. S3*A*. We define the x axis as the normal of the gold substrate and yz plane as the plane of the gold substrate. For the initial sample configuration

without any rotation ($\alpha = 0°, \beta = 0°$), pulse 1 propagates in the xy plane, and pulse 2 and pulse 3 propagate in the xz plane. All of the three pulses impinge on the sample with an initial incident angle of $\phi_0 = 10°$, and have horizontal polarization in the laboratory frame (parallel to the initial xy plane without rotation). The three excitation pulses and the echo pulse will be reflected. For the simplicity of discussion, the incident beams are treated as homogenously distributed round beams with the same radius b_0 and the electric field amplitude of each excitation pulse is set to $|\vec{E}_0| = 1$ in our simulation. Unitary wave vectors for pulse 1, 2, and 3, are expressed as $(\cos\phi_0, -\sin\phi_0, 0)$, $(\cos\phi_0, 0, -\sin\phi_0)$, and $(\cos\phi_0, 0, \sin\phi_0)$, respectively. After rotation around y and z axes, the pointing of all of the axes relative to the laboratory frame will change.

We convert the coordinates of vectors after rotation by the following relationship:

$$(x', y', z') = (x, y, z)\begin{pmatrix} \cos\beta & -\sin\beta & 0 \\ \sin\beta & \cos\beta & 0 \\ 0 & 0 & 1 \end{pmatrix}\begin{pmatrix} \cos\alpha & 0 & \sin\alpha \\ 0 & 1 & 0 \\ -\sin\alpha & 0 & \cos\alpha \end{pmatrix}. \quad \textbf{[S9]}$$

After rotation of the sample and axes, the wave vectors for pulse 1, 2, and 3 become:

Pulse 1: $(\cos\alpha\cos(\beta+\phi_0), -\sin(\beta+\phi_0), \sin\alpha\cos(\beta+\phi_0))$,

Pulse 2: $(\cos\alpha\ cos\ \beta\cos\phi_0 + \sin\alpha\sin\phi_0, -\sin\beta\cos\phi_0,\ \sin\alpha\ cos\ \beta\cos\phi_0\ - \cos\alpha\sin\phi_0)$,

Pulse 3: $(\cos\alpha\ cos\ \beta\cos\phi_0 - \sin\alpha\sin\phi_0,\ -\sin\beta\cos\phi_0,\ \sin\alpha\ cos\ \beta\cos\phi_0 + \cos\alpha\sin\phi_0)$.

Derivation of the Echo Signal Level as a Function of Rotation Angles. Because the local electric fields of excitation pulses on the monolayer surface always point along the surface normal, as shown in *The Extraction of the Average Transition Dipole Orientation Angle of Alkythiolate Monolayers on Au(111)*, the cross angle between the transition dipole of the head group and the electric fields remains constant regardless of the value of α and β. Therefore, with heterodyne detection, the observed third-order vibrational echo signal level is linear in the product of local electric fields of three excitation pulses and the number of vibrational probes in the beam area:

$$\left|\vec{E}_{echo,R}(\alpha,\beta)\right| \propto S_{overlap,R}(\alpha,\beta)\cdot\left|\vec{E}_{1,local}(\alpha,\beta)\right| \cdot\left|\vec{E}_{2,local}(\alpha,\beta)\right|\cdot\left|\vec{E}_{3,local}(\alpha,\beta)\right|, \quad \textbf{[S10]}$$

where $\vec{E}_{echo,R}$ is the electric field of the echo pulse in reflection mode, $\vec{E}_{1,local}$, $\vec{E}_{2,local}$, and $\vec{E}_{3,local}$ are the local electric fields of each pulse on surface, and $S_{overlap,R}$ is the overlap area of three pulses in reflection mode.

To numerically simulate the echo signal level, the equations that describe the projected ovals of the three pulses need to be derived. As the sample rotates, the projected oval for each pulse will remain symmetric relative to the origin of the coordinate system, but the length of the oval's long axis will change and the long axis of the oval will rotate relative to the y or z axis. The length of short axis of a projected oval is simply the radius of each incident beam, b_0. For example, for pulse 1, the projected oval on the yz plane can be specified by the length of long axis and the rotated angle of the long axis relative to y axis. Given a specific set of α and β and the wave vector of each pulse (see the previous section), we can derive the parameters that determine the projected ovals for all of the three pulses. Here, ϕ_i is the incident angle of pulse i, a_i is the length of projected oval's long axis, and γ_i is the rotation angle of the long axis relative to z axis, i = 1, 2, 3. The results for pulse 1, 2, 3 are listed in Table S1. Clockwise rotation corresponds to a negative value of $\gamma_i(\alpha,\beta)$. Based on these results, we simulated the projected ovals at each specific set of α and β. Each oval was simulated with 500 evenly spaced points and the overlap area of the three ovals, $S_{overlap,R}$, was numerically calculated.

For each pulse, the amplitude of local electric field on surface $|\vec{E}_{i,local}(\alpha,\beta)|$ is determined by the incident angle, amplitude of p-polarized component and the projected area of the pulse on sample. For a pulse with finite amount of pulse energy, the larger the projected area, the lower the electric field will be. Below, $|\vec{E}_{i,local}(\alpha,\beta)|$ is expressed by Eq. **S11**:

$$|\vec{E}_{i,local}(\alpha,\beta)| = \sqrt{\frac{\left[2\cdot\sin(\phi_i(\alpha,\beta))\cdot|\vec{E}_{i,P}(\alpha,\beta)|\right]^2}{S_i(\alpha,\beta)}} = \sqrt{\frac{\left[2\cdot\sin(\phi_i(\alpha,\beta))\cdot|\vec{E}_{i,P}(\alpha,\beta)|\right]^2}{\pi\cdot a_i(\alpha,\beta)\cdot b_0}}, \quad \textbf{[S11]}$$

where i = 1, 2, 3, $|\vec{E}_{i,P}(\alpha,\beta)|$ is the amplitude of the p-polarized electric field for pulse i, $S_i(\alpha,\beta)$ is the area of projected oval for pulse i on the rotated sample.

As stated in the previous section, the electric field amplitude of each pulse is set to be $|\vec{E}_0| = 1$. For a given set of α and β, the derived $|\vec{E}_{i,P}(\alpha,\beta)|$ for each pulse are listed in Table S1.

Until here, we have derived all of the parameters for the expression of $|\vec{E}_{echo,R}(\alpha,\beta)|$. In Fig. S3*B*, we show the simulated echo signal level covering a wide range of practical sets of α and β. The simulated echo signal is normalized by $|\vec{E}_{echo,T}|$, which is the reference signal level equivalent to the signal level of the same sample if measured in the transmission mode:

$$\left|\vec{E}_{echo,norm}(\alpha,\beta)\right| = \frac{\left|\vec{E}_{echo,R}(\alpha,\beta)\right|}{\left|\vec{E}_{echo,T}\right|} = \frac{S_{overlap,R}(\alpha,\beta)\cdot\left|\vec{E}_{1,local}(\alpha,\beta)\right|\cdot\left|\vec{E}_{2,local}(\alpha,\beta)\right|\cdot\left|\vec{E}_{3,local}(\alpha,\beta)\right|}{S_{overlap,T}\cdot\left|\vec{E}_0\right|^3}, \quad \textbf{[S12]}$$

where $S_{overlap,T}$ is the overlap area of the three pulses in transmission mode for $\alpha = 0^0$, $\beta = 0°$, and $\phi_0 = 10°$.

We sampled 100 evenly spaced angles for α and 100 evenly spaced angles for β. The corners of Fig. S3*B* are not plotted because they correspond to sample orientations that will block out at least one of the excitation pulses. As the sample is rotated, the overlap area of three pulses will increase and excite more head groups. On the other hand, the increased projected area of each pulse will cause the electric field amplitude of each pulse to decrease. Furthermore, the amplitude of local electric field for each pulse will vary to different extent, due to the changing amplitude of each pulse's p-polarized component. Overall, at $\alpha = 0^0$ and $\beta = 58°$ or $-66°$, we observe the tradeoff of the above factors gives us maximized echo signal level, which is twice as large as of the reference signal level in transmission mode. A change in α is unnecessary, because the symmetric incidence of pulse 2 and pulse 3 in BOXCARS geometry guarantees that a gain for pulse 2's local electric field will be a loss for that of pulse 3.

Molecular Dynamics Simulations

Preparation of Alkanethiol Monolayer Molecular Dynamics Simulations at Different Densities. A crystalline slab of atomic gold was constructed with the (111) facet exposed, with surface dimensions of 7.501 × 8.740 nm. The slab was four atomic layers thick in the direction normal to the surface and was held rigid during the simulation. Alkanethiol chains with $RePhen(CO)_3Cl$ head groups were attached to the gold surface on a regular grid with densities of either 1.4×10^{14} cm^{-2} or 0.7×10^{14} cm^{-2}, with these two densities chosen to match the experimentally measured head group densities. The head group was homogeneously distributed in space. Alkanethiol chains with no head groups were placed on the remaining attachment sites such that the total surface density of alkanethiol chains was 4.2×10^{14} cm^{-2}. This density was chosen to match the previously experimentally measured values for the total density of alkanethiol monolayers on gold (19). The slab and chain placement for HG_{high} and HG_{low} are shown in Fig. S4 *A* and *B*, respectively.

Parameterization of $RePhen(CO)_3Cl$ Functionalized Monolayers for Use in MD Simulations. To simulate the $RePhen(CO)_3Cl$ head group and its attached ligands, we parametrized this group for use in molecular dynamics simulations of alkanethiol monolayers. For the partial charges for phenanthroline ligand and attached rhenium complex, we used the Mulliken partial charges of gas-phase $RePhen(CO)_3Cl$ obtained from a B3LYP calculation using the 6–31+g(d,p) basis set for light atoms and the LANL2DZ pseudopotential for rhenium (16). The Lennard–Jones parameters of the phenanthroline ligand, the CO ligands and the Cl ligand were taken from the CHARMM (Chemistry at Harvard Macromolecular Mechanics) force field (33), and the Lennard–Jones parameters of the rhenium atom were chosen so as to approximate a hard sphere of radius 0.15 nm, the approximate covalent radius of neutral rhenium. Because the dynamics of interest in this study occur on a timescale of tens of picoseconds, the relaxation of the internal degrees of freedom of the phenanthroline complex, which occur on a much faster timescale, were frozen out by simulating the rhenium atom and its attached ligands as a single rigid body. The force field parameters of the $RePhen(CO)_3Cl$ are summarized in Table S2 and Fig. S5. The force field parameters for the alkanethiol chains, as well as the gold surface, were the CHARMM force field values (34).

Molecular Dynamics Simulation Details. The initial configurations of alkanethiol monolayers on gold described above were energy minimized and annealed from 500 to 300 K over 5.0 ns using a Langevin thermostat with a time constant of 1.0 ps. The resulting configuration was further equilibrated at 300 K for 35 ns with a Langevin thermostat with a time constant of 4.0 ps. After equilibration the results at each density were obtained from constant volume simulations of 20 ns using a time step of 0.5 fs. All simulations were performed using the LAMMPS (Large-scale Atomic/Molecular Massively Parallel Simulator) molecular dynamics package (35) with periodic boundary conditions used in the two dimensions parallel to the surface. Long-range Coulomb interactions were evaluated using the particle–particle, particle–mesh Ewald method with a *k*-space grid of 36 × 36 × 512 and using a slab correction method to account for the 2D periodic boundary conditions (36). The choice of *k*-space grid produced a relative error in the energy of less than 10^{-5}. A cutoff of 1.2 nm was used for real-space Coulombic and van der Waals interactions. The electric field, $E(t)$, used to compute the EECFs were calculated by projecting the average value of the electric field at the carbonyl carbons and oxygens along their respective CO bonds. The EECF is the autocorrelation function of the fluctuations in the electric field $EECF(t) = \langle \delta E(0) \delta E(t) \rangle$, where $\delta E(t) = E(t) - \langle E(t) \rangle$. Graphically identical results were obtained when using the electric field on the carbon alone or on the oxygen alone. In addition, the normalized EECF timescales obtained from the three different carbonyls differed by less than 10%; hence, an average of the three carbonyls was used as the EECF for each atom.

Decomposition of the EECFs. Because the molecular dynamics force field used here is pairwise additive, the electric field from which the EECF is obtained can be straightforwardly decomposed into contributions from different components of the system. These different components of the electric field can then be used to compute correlation functions that sum to the total EECF. In this work, we used a decomposition procedure that eliminates cross-correlation functions and has been shown to be consistent with linear response theory (29–31). Fig. S6 shows the decomposition of the EECF for the HG_{high} into its component parts (described in more detail in the main text). This decomposition reveals that the EECF of a given head group has two major contributing components that have nearly equal weights: the EECF of the phenanthroline rings of the rhenium complex anchored on the nearest-neighbor chains, and the EECF of triazole rings on the nearest-neighbor chains. The sum of all of the remaining contributions to the EECF is nearly zero. The decomposition of HG_{low} is extremely similar to the one shown in Fig. S6.

Fig. S7*B* shows that the component of the EECF that arises from neighboring head groups is extremely similar in shape and timescale to autocorrelation functions of the in-plane (wiggling) angle, ϕ_w, and the out-of-plane (wobbling) angle, θ_w. These angles are defined in Fig. S7*A*. Fig. S7 *A* and *B* therefore suggest that the electric field fluctuations of nearby head groups are caused by their motions both in and out of plane. For an arbitrary angle ζ (which may be the in-plane angle ϕ_w, the out-of-plane angle θ_w, or the triazole dihedral angle γ_d, which is described below), the angular autocorrelation function, $A(t)$ is: $A(t) = \langle \cos(\xi(0)) cos(\xi(t)) \rangle$. Fig. S7*D* shows that the portion of the EECF that comes from the triazole component is nearly identical in shape and timescale of the triazole dihedral angle autocorrelation function, which is related to rotation of the triazole ring relative to the underlying alkyl chains. The definition of the triazole dihedral γ_d is shown in Fig. S7*C*.

Increased Mass Simulations. To test whether the motions of the alkyl chains in the monolayer are related to spectral diffusion, we increased the masses of the alkyl chains by a factor of 10. In particular the mass of the all carbons, hydrogens, and sulfur atom in the alkyl chain were increased by a factor of 10. We then ran a 10-ns trajectory using the simulation procedure described in *Molecular Dynamics Simulation Details* and computed the EECFs.

Conditional EECFs. To investigate whether dihedral flips and triazole rearrangements are coupled to spectral diffusion, we computed conditional EECFs as described in the main text. In Fig. S8, a triazole rearrangement and a dihedral flip are both shown visually. The triazole rearrangement is highlighted with a dashed red circle; following a triazole rearrangement, the triazole ring has rotated to a new minimum in its dihedral potential relative to the alkyl chain. A dihedral flip is shown with a pink dashed circle, where in the left-hand side of the figure the highlighted carbon dihedral is in the gauche conformation and in the right-hand side of the figure the highlighted carbon dihedral is in the anti conformation.

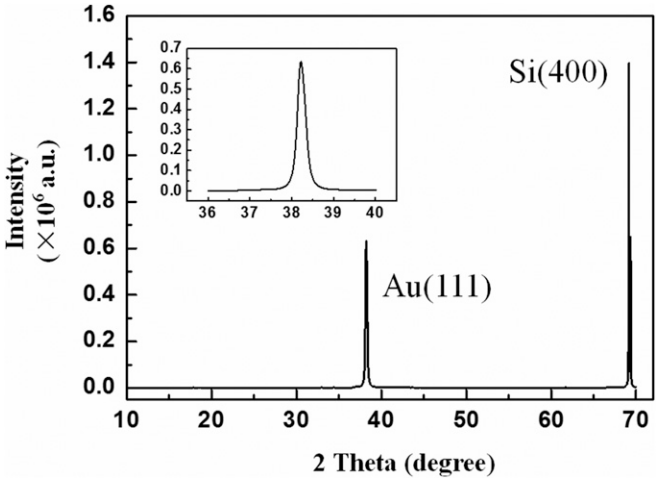

Fig. S1. XRD pattern of the Au(111) on silicon substrate. The data collection range is from 10° to 70°. *Inset* displays the zoomed-in region of the Au(111) peak.

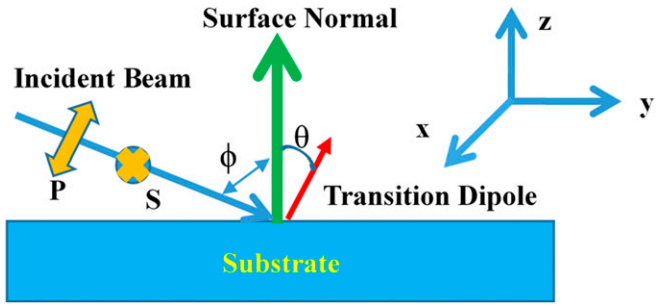

Fig. S2. An illustration showing the geometric factors related to the absorption of incident infrared beam by the anisotropic monolayer sample. The angle ϕ is the beam incident angle and the angle θ is the orientation of the transition dipole with respect to the surface normal.

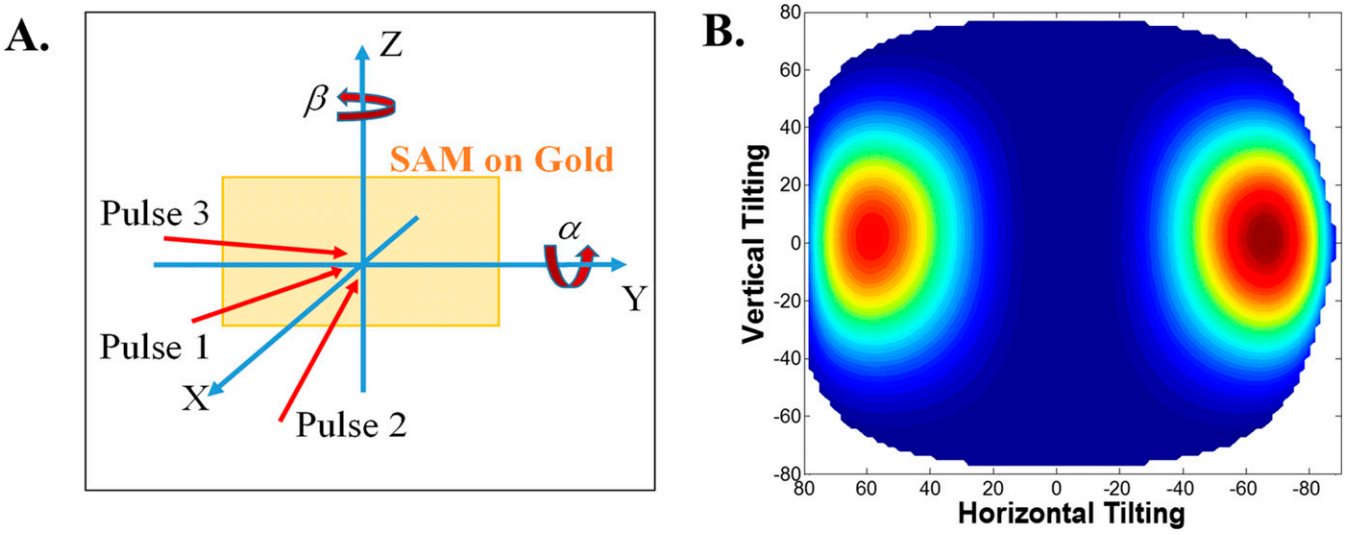

Fig. S3. (*A*) The coordinate system describing the reflection mode 2D IR. The *yz* plane is the plane of gold substrate, and *x* axis is the normal of the gold substrate. The angle α is for rotation around the horizontal *y* axis, and β is for rotation around the vertical *z* axis. The directions that correspond to positive values of α and β are indicated by the purple arrows. (*B*) Contour plot of the calculated echo signal level vs. α and β. Red indicates higher signal level, and the darkest blue in the center corresponds to no signal. The calculations show that the signal level is maximized when $\alpha = 0^0$ and $\beta = 58°$ or –66°.

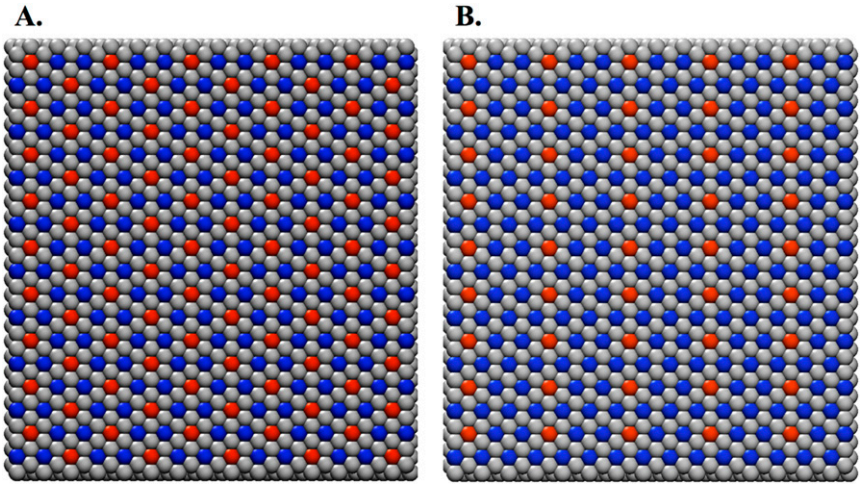

Fig. S4. Simulation setup of functionalized and unfunctionalized chains for: (*A*) The higher head group density slab and (*B*) the lower head group density slab. The view is looking down at the Au(111) plane with possible attachment sites shown as red, blue, or gray circles. Alkyl chains with RePhen$(CO)_3$Cl head groups are shown as red circles, and alkyl chains with no head groups are shown as blue circles. The gray circles represent gold atoms that are not connected to any alkyl chains.

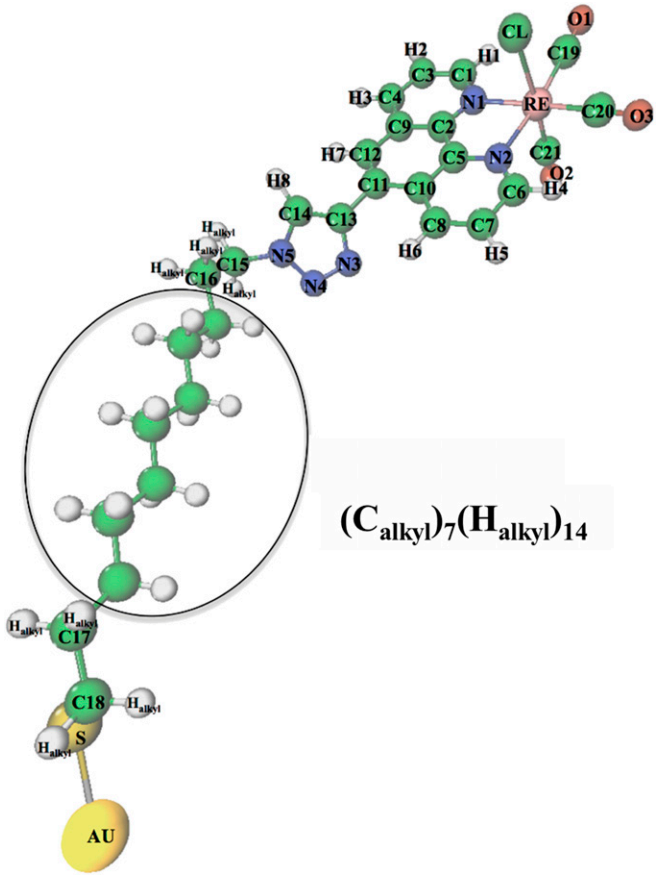

Fig. S5. Atom names for specifying force field parameters for the RePhen$(CO)_3$Cl functionalized alkanethiol chains.

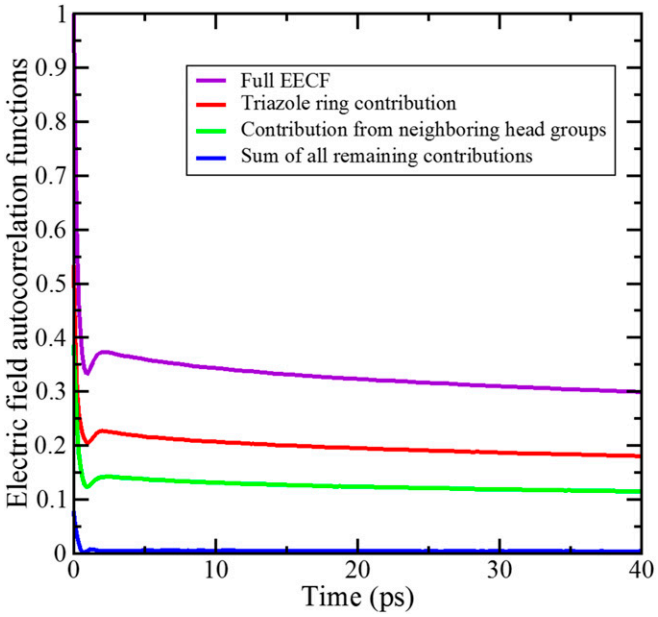

Fig. S6. Decomposition of the EECF of HG_{high} into its component parts using the decomposition scheme described in refs. 29–31. Using this scheme the full EECF (violet line) is the sum of the triazole ring contribution (red line), the contribution from nearby head groups (green line), and the sum of all remaining contributions (blue line).

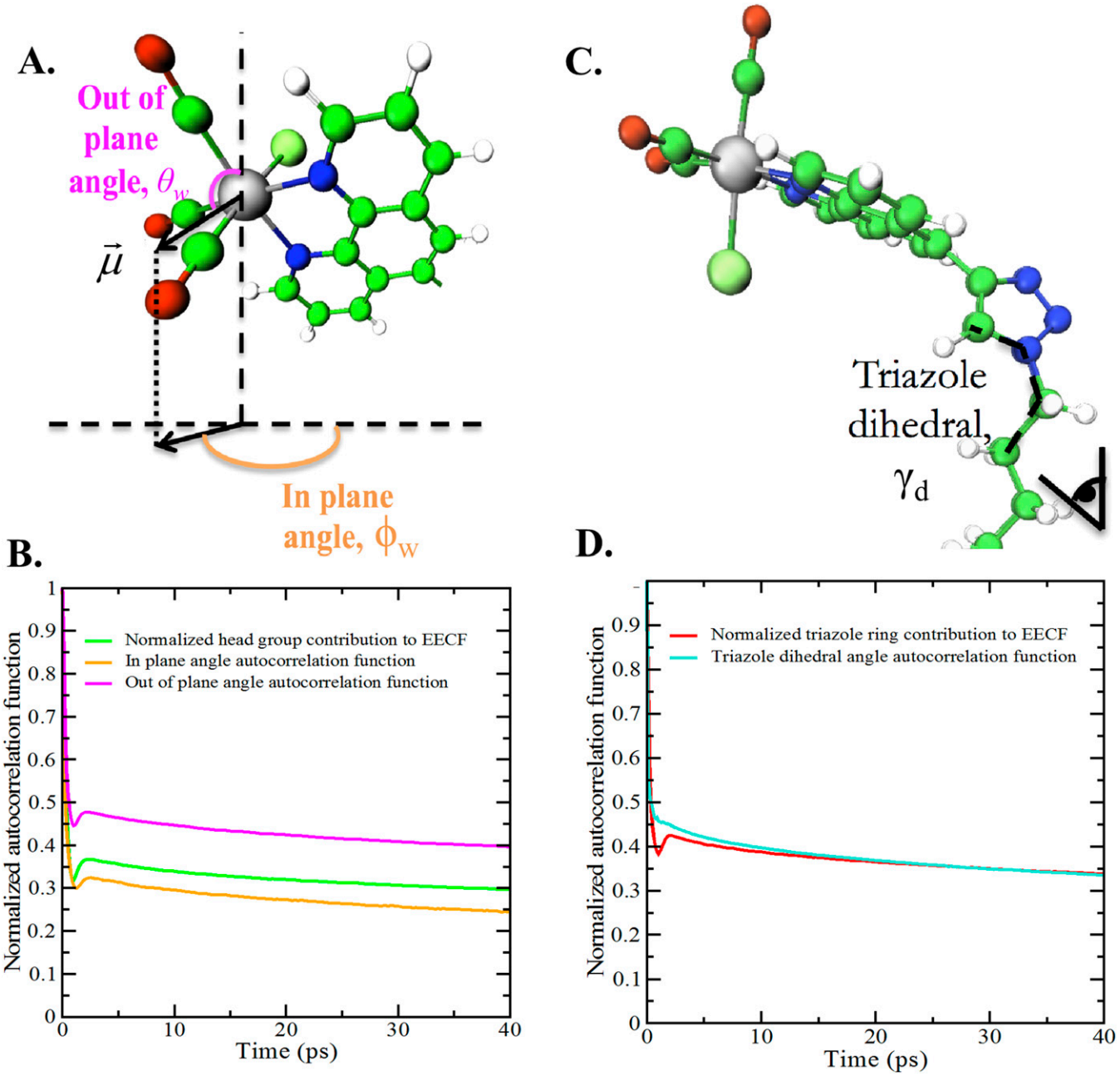

Fig. S7. (*A*) Definition of the in-plane angle ϕ_w and the out-of-plane angle θ_w of the transition dipole moment of the head group. The angle θ_w is the angle between the transition dipole moment and the surface normal, and the angle ϕ_w is obtained from the projection of the transition dipole moment vector onto the plane of the surface. (*B*) Comparison of the timescale of the neighboring head group contribution to the EECF and the angular correlation functions of head group motion. (*C*) Definition of the triazole dihedral angle, γ_d. (*D*) Comparison of the timescale of the triazole ring contribution to the EECF (shown normalized here) and the triazole dihedral angle autocorrelation function.

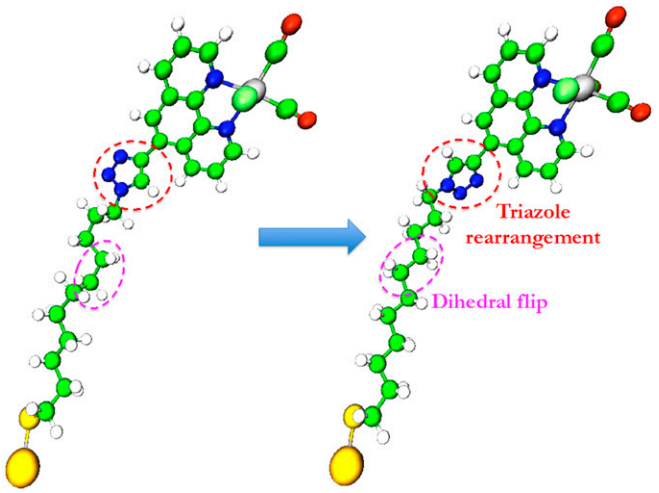

Fig. S8. Visualization of events used in conditional correlation functions. A triazole rearrangement is highlighted in the red dashed circle, and a dihedral flip is highlighted inside the pink dashed circle. For visual clarity, only a single chain is shown.

Table S1. Parameter expressions for the three excitation pulses as the function of tilt angles

Variable	Expression in terms of α and β
$\phi_1(\alpha,\beta)$	$\lvert\arccos(\cos\alpha\cos(\beta+\phi_0))\rvert$
$a_1(\alpha,\beta)$	$\frac{b_0}{\cos(\phi_1(\alpha,\beta))}$
$\gamma_1(\alpha,\beta)$	$-\arctan\left(\frac{\sin\alpha\cos(\beta+\phi_0)}{\sin(\beta+\phi_0)}\right)$
$\phi_2(\alpha,\beta)$	$\lvert\arccos(\cos\alpha\cos\beta\cos\phi_0+\sin\alpha\sin\phi_0)\rvert$
$a_2(\alpha,\beta)$	$\frac{b_0}{\cos(\phi_2(\alpha,\beta))}$
$\gamma_2(\alpha,\beta)$	$\arctan\left(\frac{\sin\beta\cos\phi_0}{\sin\alpha\cos\beta\cos\phi_0-\cos\alpha\sin\phi_0}\right)$
$\phi_3(\alpha,\beta)$	$\lvert\arccos(\cos\alpha\cos\beta\cos\phi_0-\sin\alpha\sin\phi_0)\rvert$
$a_3(\alpha,\beta)$	$\frac{b_0}{\cos(\phi_3(\alpha,\beta))}$
$\gamma_3(\alpha,\beta)$	$\arctan\left(\frac{\sin\beta\cos\phi_0}{\sin\alpha\cos\beta\cos\phi_0+\cos\alpha\sin\phi_0}\right)$
$\lvert\vec{E}_{1,P}(\alpha,\beta)\rvert$	$\left\lvert\frac{\cos\alpha\sin(\beta+\phi_0)}{\sqrt{1-\cos^2\alpha\cos^2(\beta+\phi_0)}}\right\rvert$
$\lvert\vec{E}_{2,P}(\alpha,\beta)\rvert$	$\left\lvert\frac{\cos\alpha\sin\beta}{\sqrt{\sin^2\alpha\cos^2\beta\cos^2\phi_0+\cos^2\alpha\sin^2\phi_0+\sin^2\beta\cos^2\phi_0-2\sin\alpha\cos\alpha\cos\beta\sin\phi_0\cos\phi_0}}\right\rvert$
$\lvert\vec{E}_{3,P}(\alpha,\beta)\rvert$	$\left\lvert\frac{\cos\alpha\sin\beta}{\sqrt{\sin^2\alpha\cos^2\beta\cos^2\phi_0+\cos^2\alpha\sin^2\phi_0+\sin^2\beta\cos^2\phi_0+2\sin\alpha\cos\alpha\cos\beta\sin\phi_0\cos\phi_0}}\right\rvert$

Table S2. Molecular dynamics simulation parameters for the RePhen(CO)$_3$Cl head group

Atom name	Lennard–Jones σ(Å)	Lennard–Jones ε (kcal/mol)	Lennard–Jones 1–4 σ(Å)	Lennard–Jones 1–4 ε (kcal/mol)	Charge (e)
N1	0.06	3.367597	0.06	3.367597	−0.552314
C1	0.07	3.550053	0.07	3.550053	0.069506
C2	0.07	3.550053	0.07	3.550053	0.287538
C3	0.07	3.550053	0.07	3.550053	−0.157534
H1	0.046	1.959977	0.046	1.959977	0.189856
C4	0.07	3.550053	0.07	3.550053	−0.151167
H2	0.03	2.420037	0.03	2.420037	0.161009
H3	0.03	2.420037	0.03	2.420037	0.160862
N2	0.06	3.367597	0.06	3.367597	−0.550709
C5	0.07	3.550053	0.07	3.550053	0.267022
C6	0.07	3.550053	0.07	3.550053	0.073985
C7	0.07	3.550053	0.07	3.550053	−0.158976
H4	0.046	1.959977	0.046	1.959977	0.190486
C8	0.07	3.550053	0.07	3.550053	−0.163936
H5	0.03	2.420037	0.03	2.420037	0.158021
H6	0.03	2.420037	0.03	2.420037	0.152211
C9	0.07	3.550053	0.07	3.550053	0.169259
C10	0.07	3.550053	0.07	3.550053	0.118201
C11	0.07	3.550053	0.07	3.550053	0.088106
C12	0.07	3.550053	0.07	3.550053	−0.264341
H7	0.03	2.420037	0.03	2.420037	0.168746
C13	0.05	3.741775	0.05	3.741775	0.116796
C14	0.05	3.741775	0.05	3.741775	−0.019628
H8	0.046	1.603618	0.046	1.603618	0.17881
N3	0.2	3.296325	0.2	3.296325	−0.304076
N4	0.2	3.296325	0.2	3.296325	0.122795
C15	0.056	3.581413	0.01	3.385415	−0.276186
C16	0.056	3.581413	0.01	3.385415	−0.186069
N5	0.2	3.296325	0.2	3.296325	0.458982
C_{alkyl}	0.056	3.581413	0.01	3.385415	−0.201575
H_{alkyl}	0.035	2.387609	0.035	2.387609	0.086965
C17	0.056	3.581413	0.01	3.385415	−0.184002
C18	0.056	3.581413	0.01	3.385415	−0.189171
CL	0.1	4.400000	0.1	4.400000	−0.341736
RE	1.00E-06	4.000135	1.00E-06	4.000135	0.319741
C19	0.11	3.741775	0.11	3.741775	0.17511
O1	0.12	3.029056	0.12	3.029056	−0.301221
C20	0.11	3.741775	0.11	3.741775	0.174967
C21	0.11	3.741775	0.11	3.741775	0.140205
O2	0.12	3.029056	0.12	3.029056	−0.317974
O3	0.12	3.029056	0.12	3.029056	−0.302639
S	0.45	3.563595	0.45	3.563595	−0.115776
AU	0.039	2.933729	0.039	2.933729	0